

Electronic Supplementary Material (ESI) for Journal of Materials Chemistry C.
This journal is © The Royal Society of Chemistry 2018

Electronic Supplementary Information

Anisotropic electrical and magnetic properties in grain-oriented $\text{Bi}_4\text{Ti}_3\text{O}_{12}\text{-La}_{0.5}\text{Sr}_{0.5}\text{MnO}_3$

Wei Zou,^a Jianlin Wang,^{*bc} Zezhi Chen,^a Nai Shi,^a Zhiang Li,^a Zhangzhang Cui,^a Xiaoning Li,^a Xiaofeng Yin,^a Wensheng Yan,^b Haoliang Huang,^b Ranran Peng,^a Zhengping Fu,^{*ac} Yalin Lu^{*abc}

^aDepartment of Materials Science and Engineering, University of science and Technology of China, Hefei 230026, Anhui, China

^bNational Synchrotron Radiation Laboratory, University of Science and Technology of China, Hefei 230026, Anhui, China

^cSynergetic Innovation Center of Quantum Information & Quantum Physics, Hefei National Laboratory for Physical Sciences at the Microscale, University of Science and Technology of China, Hefei 230026, Anhui, China

*Email of corresponding authors: wangjl@ustc.edu.cn, fuzp@ustc.edu.cn, yllu@ustc.edu.cn

Contents:

Fig. S1. BIT-LSMO nanoparticle synthesized at different temperatures by hydrothermal method.....3

Fig. S2. BIT-LSMO nanoparticle synthesized at different KOH concentrations by hydrothermal method5

Fig. S3. Grain-oriented BIT-LSMO ceramics sintered at different temperatures by muffle furnace.....7

Table S1. The calculation of Lotgering Factor for MF and HP samples9

Fig. S4. Using the “Brick Layer” model to estimate the total conductivity caused by grain interiors and grain boundaries of MF and HP samples.....10

Fig. S5. Electrochemical impedance spectroscopy of MF sample12

Fig. S6. Hall measurement of the MF sample13

Fig. S7. Using the CTM4XAS to calculate the Mn L edge XAS14

1. BIT-LSMO nanoparticle synthesized at different temperatures by hydrothermal method

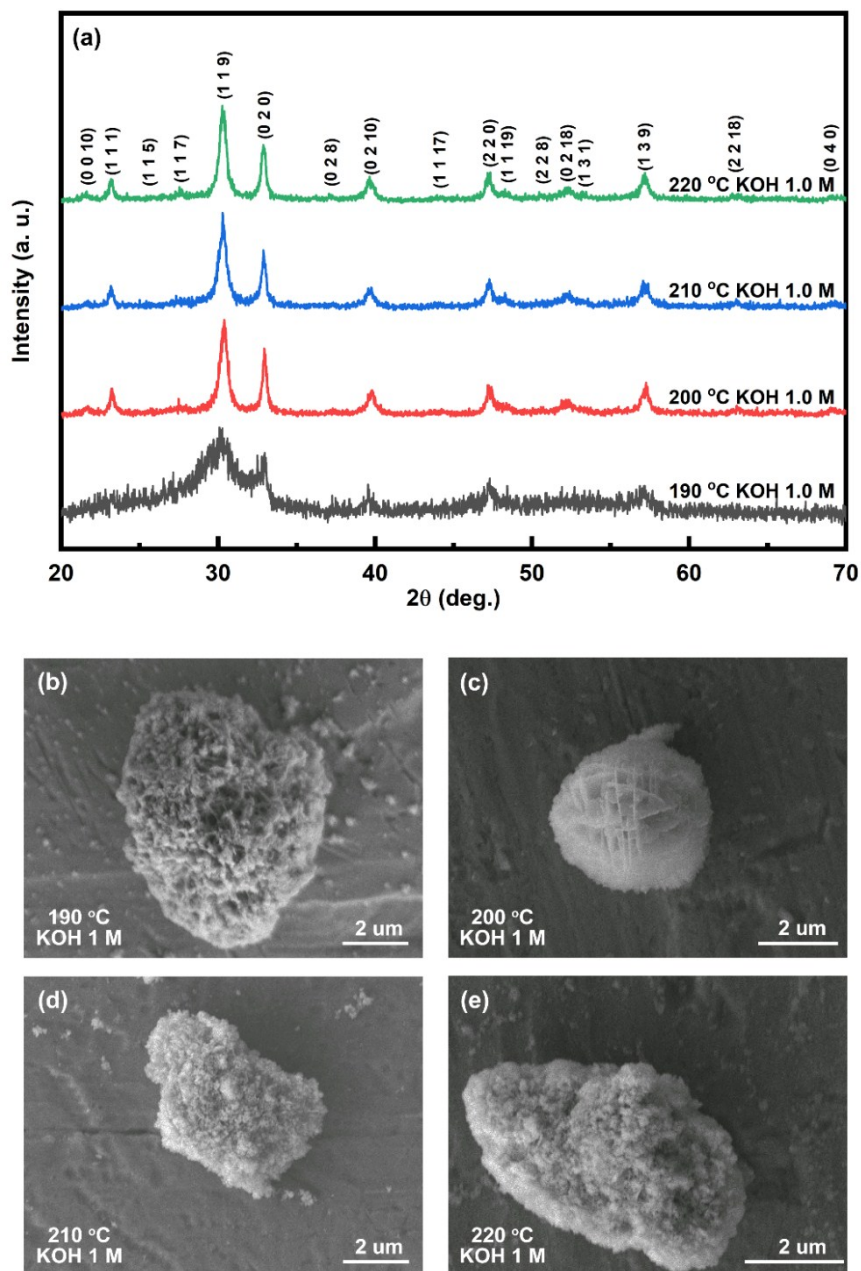


Fig. S1. (a) XRD patterns and (b-e) SEM images of the BIT-LSMO samples synthesized by hydrothermal method at 190 °C, 200 °C, 210 °C, 220 °C, respectively.

Since temperature is the key factor in hydrothermal process, we set a temperature series of 190 °C, 200 °C, 210 °C, 220 °C to optimize the temperature for hydrothermal synthesis. A moderate KOH concentration of 1 M and reaction time of 48 h were chosen initially to explore the effects of temperature. Fig. S1a shows X-ray diffraction patterns of the powders synthesized under different hydrothermal temperatures. At 190 °C, the diffraction peaks have many glitches and quite large FWHM, indicating poor crystallinity. When the temperature is higher than 200 °C, the glitches

diminish and the peaks become sharp. The patterns at 200 °C, 210 °C, 220 °C are similar. We contrast the XRD patterns here with that of BIT-LSMO ceramics synthesized by conventional solid state reaction method in our previous work¹ and they coordinate well. The Miller Index of main diffraction peaks are denoted correspondingly. Fig. S1 (b-d) shows the morphology of particles synthesized at different temperatures. At 190 °C, the formation of BIT-LSMO begins, but it has a poor crystallinity. At 200 °C, the morphology is nanoflower formed by crossed nanoplates. At 210 °C and 220 °C, the nanoflower changes into irregular lump because of agglomeration as temperature increases. So we chose 200 °C, 48 h as the follow-up growth condition.

2. BIT-LSMO nanoparticle synthesized at different KOH concentrations by hydrothermal method

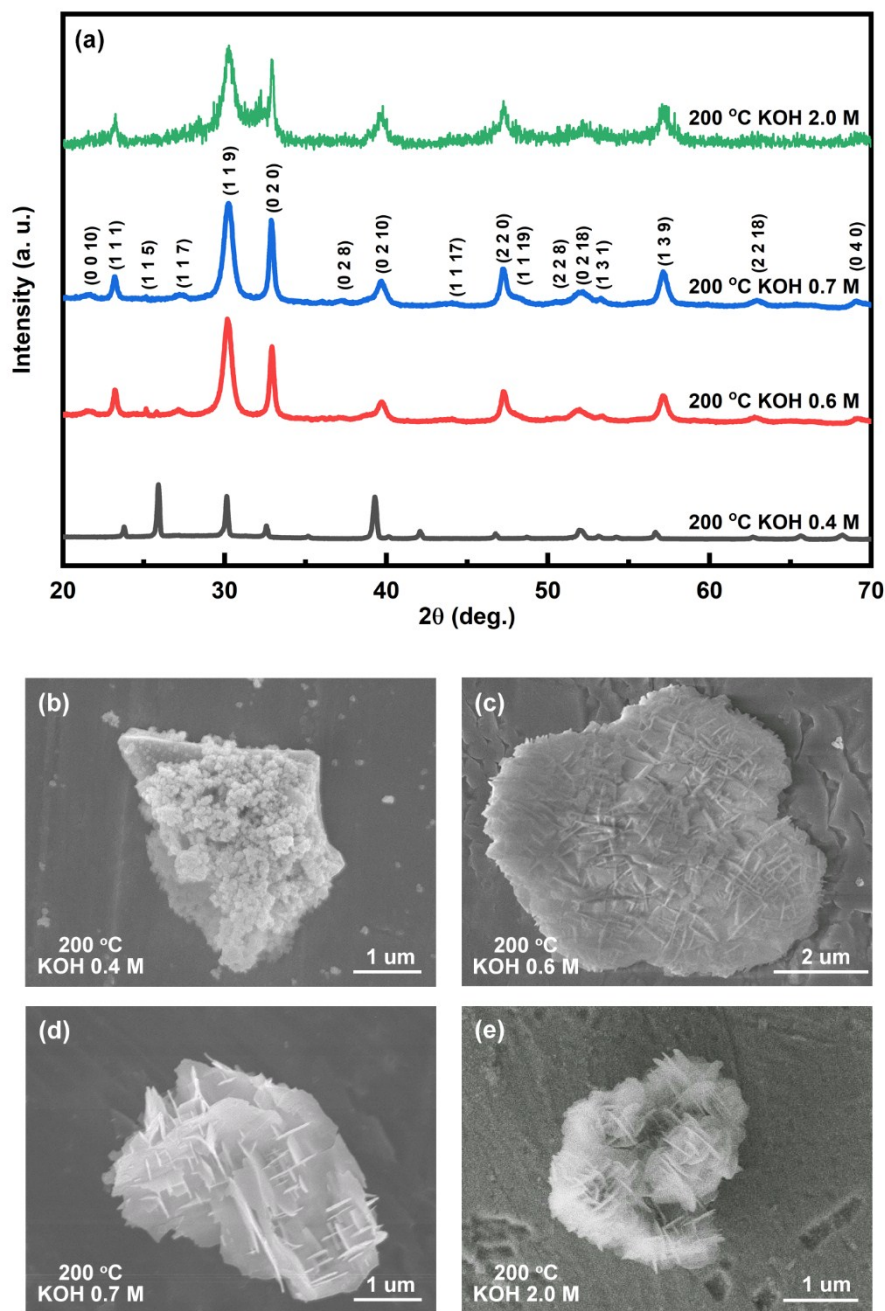


Fig. S2. (a) XRD patterns and (b-e) SEM images of the BIT-LSMO samples synthesized by hydrothermal method at different KOH concentrations of 0.4 M, 0.6 M, 0.7 M, 2.0 M, respectively.

The alkali concentration is also a very important factor in hydrothermal process besides temperature. Fig. S2 reflects how the concentration of KOH influences the growth of BIT-LSMO. Fig. S2a shows the XRD patterns of samples synthesized under different KOH concentrations. At 0.4 M, the product is pure phase $\text{Bi}_2\text{O}_2\text{CO}_3$ (all diffraction peaks are well assigned according to

JCPDS 41-1488). At 0.6 M, the product is mainly BIT-LSMO, but there is an impurity diffraction peak at about $2\theta = 25.1^\circ$. At 0.7 M, the impurity peak disappears, indicating pure phase BIT-LSMO. When the KOH concentration elevates to 2 M, an impurity peak at $2\theta = 32.2^\circ$ appears. So at the KOH concentration around 0.7 to 1.0 M, combined with the former optimized temperature of 200 °C, pure BIT-LSMO is obtained. According to Fig. S2 (b-e), the nanoflower begins to form at 0.6 M and grows up at 0.7 M. However, with the KOH concentration increasing, the nanoflower becomes smaller as shown in SEM images in Fig. S2d, S1c, and S2e. Finally, we chose 0.7 M KOH, 200 °C 48 h as the optimum hydrothermal condition for BIT-LSMO growth.

3. Grain-oriented BIT-LSMO ceramics sintered at different temperatures by muffle furnace

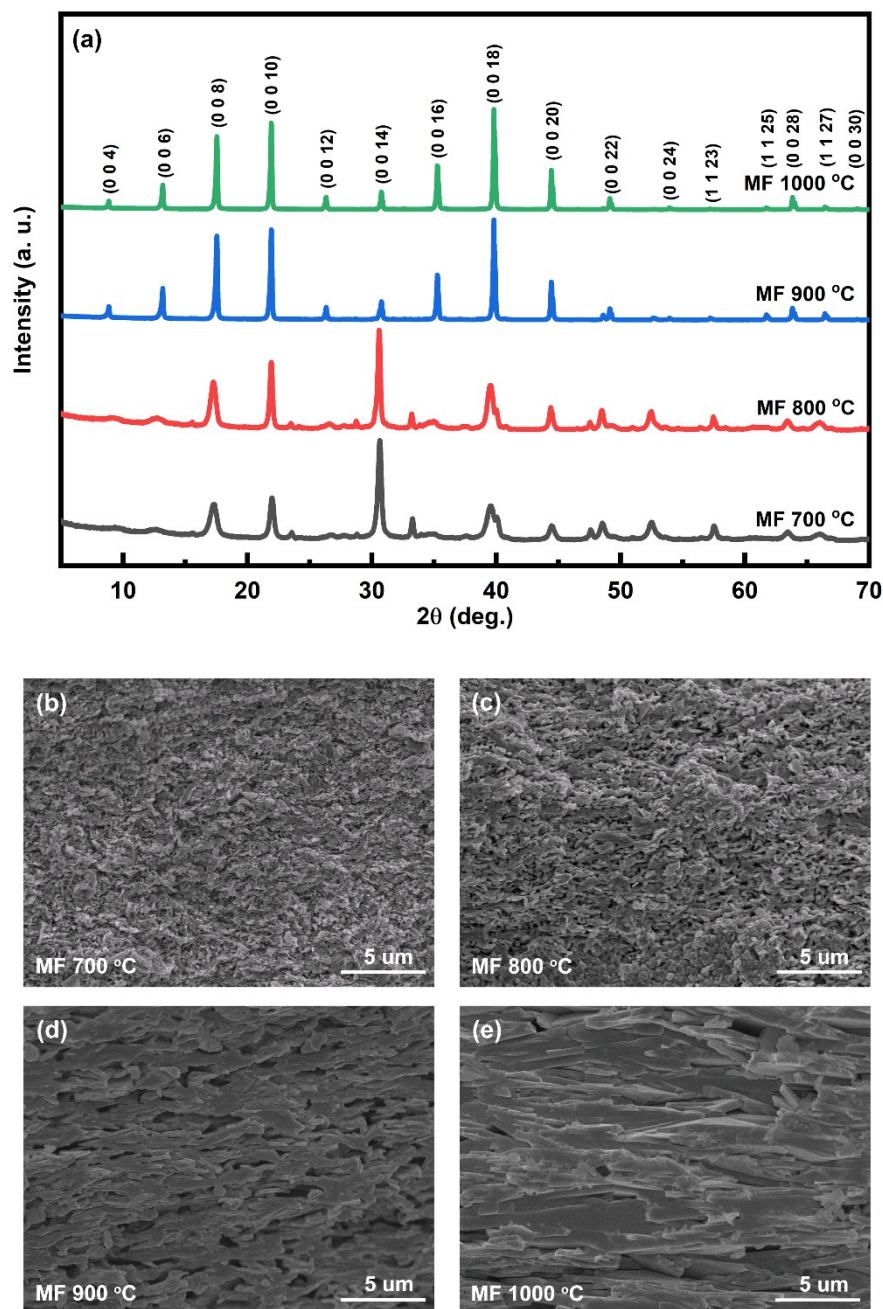


Fig. S3. (a) XRD patterns of muffle-calcined ceramics at different temperatures; SEM images of (b) 700 °C (c) 800 °C (d) 900 °C (e) 1000 °C muffle-calcined BIT-LSMO ceramics

We use the hydrothermal nanoparticles as precursor to synthesize grain-oriented ceramics. Fig. S3a illustrates the XRD patterns of ceramics sintered at different temperatures. For the samples sintered at 700 °C and 800 °C, the dominating diffraction peak is still (1 1 9), while for the samples sintered at 900 °C and 1000 °C, the dominating diffraction peak changes into (0 0 18) which

indicates a preferential orientation. The SEM image in Fig. S3 (b-g) agrees with the conclusion. The orientation and morphology change at different stages from SEM images.

4. The calculation of Lotgering Factor for MF and HP samples

To evaluate the degree of preferred grain orientation in the prepared ceramics, the Lotgering Factor is applied²: $LF = \frac{(p - p_0)}{(1 - p_0)}$, where p is the value of sum of all orientation related peak intensity divided by sum of all peak intensity in the oriented sample, and p_0 is that in the randomly oriented sample. The LF of both 1000 °C muffle and hot-press calcined sample tend to be 1 since most recognizable peaks are oriented related in the corresponding patterns (which cause p nearly to be 1), which means a very good preferred orientation, we calculate the LF precisely. The calculated LF values for MF and HP samples are 98.69% and 99.87%, respectively.

Table S1. The calculation of Lotgering Factor

Peaks	Samples	MF 1000 °C	HP 1000 °C		HT
(0 0 4)		0.0854	0.1576	(0 0 8)	0.0483
(0 0 6)		0.2454	0.3377	(0 0 10)	0.0977
(0 0 8)		0.7290	0.8427	(1 1 1)	0.3403
(0 0 10)		0.8636	0.8471	(1 1 5)	0.0623
(0 0 12)		0.1255	0.1383	(1 1 7)	0.0927
(0 0 14)		0.1766	0.2038	(1 1 9)	1.0000
(0 0 16)		0.4383	0.4451	(0 2 0)	0.9454
(0 0 18)		1.0000	1.0000	(0 2 8)	0.0583
(0 0 20)		0.3935	0.3458	(0 2 10)	0.2330
(0 0 22)		0.1121	0.1024	(1 1 17)	0.0373
(0 0 24)		0.0204	0.0197	(2 2 0)	0.4196
(1 1 23)		0.0073	0.0019	(1 1 19)	0.0839
(1 1 25)		0.0200	0.0038	(2 2 8)	0.0465
(0 0 28)		0.1231	0.1093	(0 2 18)	0.1309
(1 1 27)		0.0278	-	(1 3 1)	0.0806
(0 0 30)		0.0052	-	(1 3 9)	0.3421
				(2 2 18)	0.0608
				(0 4 0)	0.0636
all peak sum		4.3732	4.5552	all peak sum	4.1433
(0 0 n) peak sum		4.3181	4.5495	(0 0 n) peak sum	0.1460
p		0.9874	0.9987	p ₀	0.0352
Lotgering Factor		0.9869	0.9987		

5. Using the “Brick Layer” model to estimate the total conductivity caused by grain interiors and grain boundaries of MF and HP samples

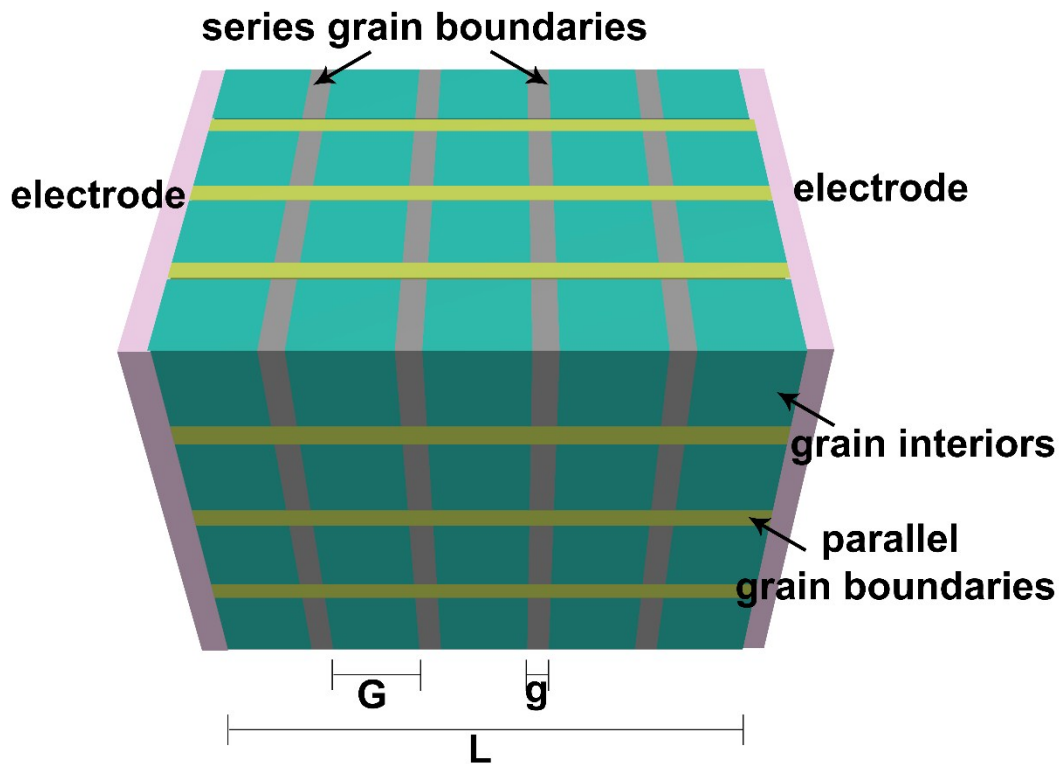


Fig. S4. The “Brick Layer” model

Use the “Brick Layer” model³⁻⁵ illustrated in Fig. S4, we can get the equation below:

$$\sigma_1 = (2\eta \cdot \sigma_{gb} + \sigma_{gi}) \quad (S1)$$

$$\sigma_2 = \frac{\sigma_{gb}}{\eta} \quad (S2)$$

$$\frac{\sigma_1}{\sigma_2} = 2\eta^2 + \eta \cdot \frac{\sigma_{gi}}{\sigma_{gb}} \quad (S3)$$

Since η (defined as the ratio of grain boundaries thickness in the current transmission direction to the total transmission path length) is very small (about at the magnitude of 0.001), and $\sigma_{gi} > \sigma_{gb}$, the equation can be simplified as

$$\sigma_1 = \sigma_{gi} \quad (S4)$$

$$\frac{R_2}{R_1} = \frac{\sigma_1}{\sigma_2} = \eta \cdot \frac{\sigma_{gi}}{\sigma_{gb}} \quad (S5)$$

And obviously, we have

$$\frac{1}{\sigma} = \frac{1}{\sigma_1} + \frac{1}{\sigma_2} \quad (\text{S6})$$

So the total conductivity can be obtained:

$$\sigma = \sigma_{gi} / \left(1 + \eta \cdot \frac{\sigma_{gi}}{\sigma_{gb}} \right) \quad (\text{S7})$$

6. Electrochemical impedance spectroscopy

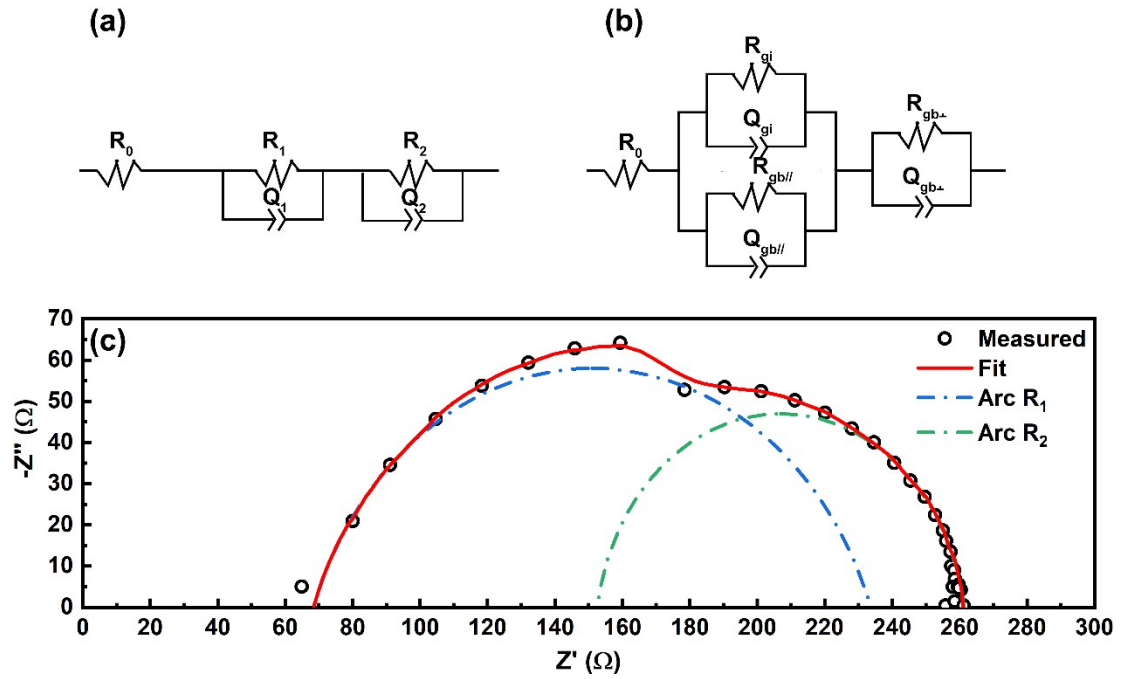


Fig. S5. (a)(b) The equivalent circuits of our sample (c) Nyquist plot of MF sample, measured at 473 K.

We use the electrochemical impedance spectroscopy to extract the conductivity contributed by grain interiors and grain boundaries.³ Fig. S5a and S5b are the equivalent circuits we used for the sample. R denotes resistor and Q denotes constant phase element. Fig. S5c is the Nyquist diagram of our MF sample. The curve can be divided into two semicircles, the Arc R_1 in the higher frequency area can be attributed to the grain interiors and parallel grain boundaries, the Arc R_2 in the lower frequency area can be attributed to the perpendicular grain boundaries. From the extracted value of $R_1/R_2 = 6.11$ and $\eta = 0.004$ estimated by SEM image, with Equa. S5, we can get $\sigma_{gb}/\sigma_{gi} = 0.024$.

7. Hall measurement of the MF sample

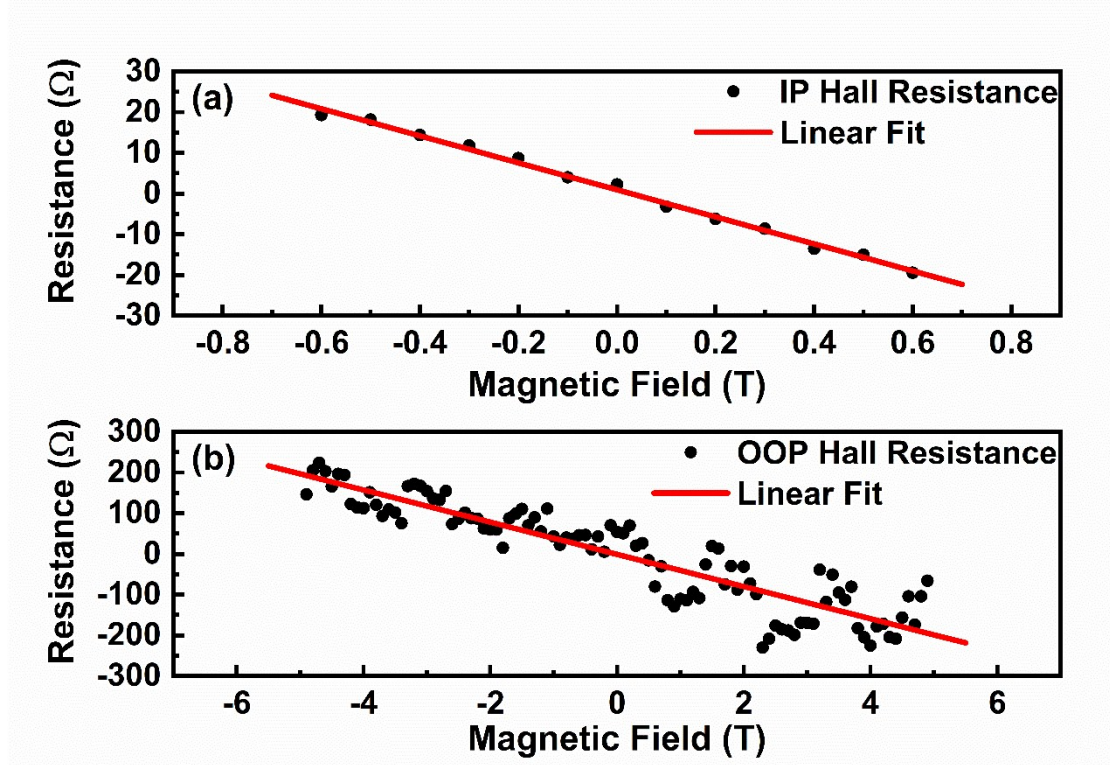


Fig. S6. (a) IP Hall resistance measurement results of the MF sample (b) OOP Hall resistance measurement results of the MF sample.

For Hall measurement, we have the equations below:

$$n = \frac{BI}{edV_H} \quad (\text{S8})$$

$$\mu = \frac{1}{ne\rho} \quad (\text{S9})$$

In which n denotes the carrier density, B denotes the magnetic field, I denotes the current, e denotes the electronic charge, d denotes the thickness of the sample, V_H denotes the Hall voltage.

And the measured slope k in Fig. S6 satisfies the following equation:

$$k = \frac{R}{B} = \frac{V_H}{IB}, \quad (\text{S10})$$

So we can get

$$n = \frac{1}{edk} \quad (\text{S11})$$

Then, we can calculate out the carrier density and Hall mobility with the results of $p_{\text{IP}} = 3.42 \times 10^{14} \text{ cm}^{-3}$, $p_{\text{OOP}} = 3.16 \times 10^{14} \text{ cm}^{-3}$, $\mu_{\text{IP}} = 0.269 \text{ cm}^2 \cdot \text{V}^{-1} \cdot \text{s}^{-1}$ and $\mu_{\text{OOP}} = 0.037 \text{ cm}^2 \cdot \text{V}^{-1} \cdot \text{s}^{-1}$.

8. Using the CTM4XAS⁶ to calculate the Mn L edge XAS

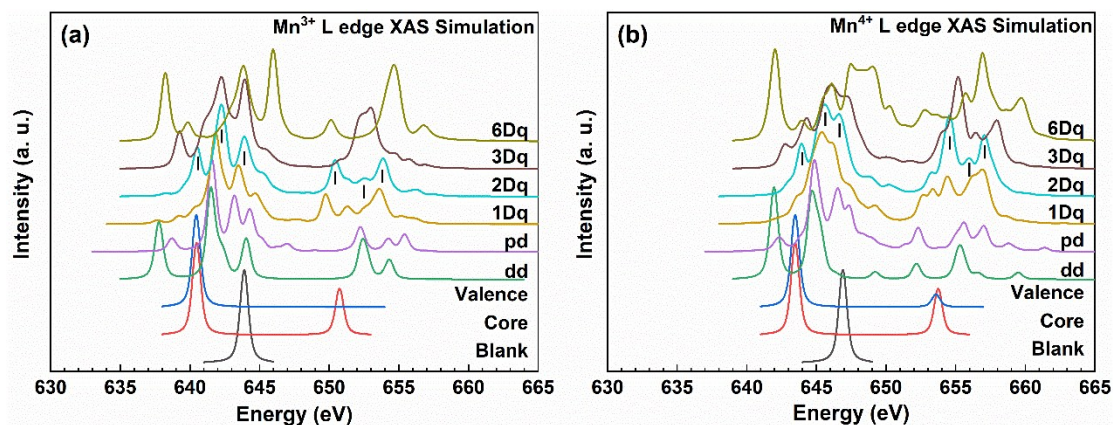


Fig. S7. The calculated XAS of (a) Mn^{3+} L edge (b) Mn^{4+} L edge, taking different factors into account.

To explore the Mn electron states, we use the CTM4XAS software to calculate the XAS of Mn^{3+} and Mn^{4+} under different conditions. From the bottom to top, we add the core spin-orbit coupling, valence spin-orbit coupling, d-d electrons coupling, coupling of the core state and valence state, and the crystal field splitting effect one by one. The absorption spectrum is dominated by dipole transitions from the core 2p level to the empty 3d states (from the ground $3d^n$ state to the $2p^5 3d^{n+1}$ final states). We label the peaks in Fig. S5a and Fig. S5b with short straight lines below as A, B, C, D, E, F from left to right. For both Mn^{3+} and Mn^{4+} , the core spin-orbit coupling causes the main split to L_3 (A, B, C) (with an initial state of $2p_{3/2}$) and L_2 (D, E, F) (with an initial state of $2p_{1/2}$) branches. Peak B and C are caused by spin-orbit and d-d, p-d coupling, and peak A is related to crystal field caused splitting. We contrast the peak shape here and our experimental data in Fig. 7b, the 10Dq parameter in our experiment is most likely to be between 1 eV and 2 eV. We can see from Fig. S5a and Fig. S5b clearly that with the increase of 10Dq, the ratio of peak A to peak B and C gets smaller, and the conclusion explains the peak A changing trend in Fig. 7b.

References

1. J. Wang, Z. Chen, H. Huang, J. Cui, W. Zhang, Z. Fu, R. Peng, W. Yan and Y. Lu, *Appl. Phys. Lett.*, 2017, **110**, 212102.
2. R. Furushima, S. Tanaka, Z. Kato and K. Uematsu, *J. Ceram. Soc. Jpn.*, 2010, **118**, 921–926.
3. S. M. Haile, D. L. West and J. Campbell, *J. Mater. Res.*, 1998, **13**, 1576–1595.
4. G. M. Christie and F. P. F. van Berkel, *Solid State Ion.*, 1996, **83**, 17–27.
5. H. Nafe, *Solid State Ion.*, 1984, **13**, 255–263.
6. E. Stavitski and F. M. F. de Groot, *Micron*, 2010, 41, 687–694.